Available online at www.sciencedirect.com
ScienceDirect
Journal of Catalysis 249 (2007) 349–358
JOURNAL OF CATALYSIS
www.elsevier.com/locate/jcat

A Pd-doped perovskite catalyst, $BaCe_{1-x}Pd_xO_{3-\delta}$, for CO oxidation

Udayshankar G. Singh [a,b], Jun Li [c], Joseph W. Bennett [d], Andrew M. Rappe [d,*], Ram Seshadri [c,*], Susannah L. Scott [a,b,*]

[a] *Department of Chemical Engineering, University of California, Santa Barbara, CA 93106, USA*
[b] *Department of Chemistry and Biochemistry, University of California, Santa Barbara, CA 93106, USA*
[c] *Materials Department, and Materials Research Laboratory, University of California, Santa Barbara, CA 93106, USA*
[d] *The Makineni Theoretical Laboratories, Department of Chemistry, University of Pennsylvania, Philadelphia, PA 19104-6323, USA*

Received 25 January 2007; revised 1 April 2007; accepted 25 April 2007

Available online 19 June 2007

Abstract

Perovskite $BaCeO_3$ materials with low levels of substitution of Pd(II) on the Ce site and a corresponding number of oxygen vacancies were prepared by a high-temperature synthesis method. Although their surface areas are low (ca. 1.0 $m^2\ g^{-1}$), their low-temperature (<200 °C) activity for CO oxidation is comparable to that of highly dispersed PdO/Al_2O_3. When the doped perovskites are reduced extensively in H_2, causing extrusion of Pd(0) from the lattice, their catalytic activity declines dramatically. Consequently, activity is attributed to the presence of cationic Pd(II) in the perovskite lattice. Density functional theory was used to investigate the atomic and electronic character of the structures containing oxygen vacancies. Both experimental and theoretical evidence support a catalytic mechanism involving labilization of lattice and surface oxygen by cationic Pd(II).

Keywords: Perovskite; Palladium; CO oxidation; Cation mobility; Oxygen mobility; Oxygen vacancy; DFT

1. Introduction

Noble-metal-promoted perovskites have been studied for potential use as automobile exhaust catalysts since the 1970s [1–3]. Incorporation of these metals into a perovskite structure can prevent their sintering, reduce losses due to volatilization at high operating temperatures, and avoid reactions with the support that lead to catalyst deactivation. Despite these advantages, however, commercial implementation of perovskite catalysts has been slow, due to their low moisture and sulfur tolerance [4]. More recently, the decline in three-way activity at high temperatures has been linked to the ability of the perovskites to catalyze the water–gas shift and steam-reforming reactions [5].

Recently, researchers at Daihatsu described a family of noble-metal-doped perovskites that they termed "intelligent catalysts" [6]. When these materials are used in catalytic converters, environmental fluctuations due to the engine cycle cause Pd to migrate into and out of the perovskite reservoir. Pd ions present in the perovskite matrix $LaFe_{0.57}Co_{0.38}Pd_{0.05}O_3$ were proposed to be in equilibrium with nanoparticles of Pd–Co alloy on the surface. A Co-free system, $LaFe_{0.95}Pd_{0.05}O_3$, generates Pd-only nanoparticles [7]. The activity for NO_x reduction by H_2 is associated with the presence of these nanoparticles, with diameters <2 nm, on the perovskite surface [8]. Three-way activity under near-stoichiometric reaction conditions was attributed to Pd(0) nanoparticles dispersed on the surface of $LaFe_{0.8}Co_{0.2}O_3$ [9]. The perovskite support exerts a dramatic effect on metal particle sintering; during thermal aging sufficient to cause irreversible coarsening for Pd(0) supported on alumina, the perovskite-stabilized Pd or Pd–Co nanoparticles are stable. Some of these materials are now in commercial use [10], resulting in a 70% decrease in precious metal usage compared with conventional automotive catalysts [11].

* Corresponding authors. Fax: +1 805 893 4731.
E-mail addresses: rappe@sas.upenn.edu (A.M. Rappe), seshadri@mrl.ucsb.edu (R. Seshadri), sscott@engineering.ucsb.edu (S.L. Scott).

0021-9517/$ – see front matter
doi:10.1016/j.jcat.2007.04.023

The activity of the methane combustion catalyst $LaMn_xFe_{1-x}O_3$ is also promoted by the presence of noble metals such as Pd, Pt, and Rh [12,13]. In these systems, the perovskite has been suggested to serve as a support for highly dispersed PdO particles in the oxidizing reactive atmosphere [14]. The role of the perovskite was inferred to be the prevention of sintering of the active PdO phase [15] via the reversible formation of a perovskite solid solution [12]. In other cases, the enhanced reactivity of noble-metal-promoted perovskite catalysts has been attributed to the perovskite phase itself. For example, the high-temperature activity for lean NO_x reduction has been linked to the presence of ionic Pd in a $LaCoO_3$ matrix [16]. No evidence for metallic Rh has been found during the partial oxidation of methane to syn gas under fuel-rich conditions by Rh–$LaMnO_3$ [17]. Thus, activity has been attributed to the mixed-oxide phase.

Recently, we showed that $BaCeO_3$ can incorporate low levels of Pd(II) on the B sites, and that Pd moves reversibly out of and back into the lattice in response to strongly reducing or oxidizing conditions, respectively [18]. The host $BaCeO_3$ was chosen to accommodate the large Pd cation on the B site of the perovskite lattice, while providing redox flexibility and oxygen-storage capacity (OSC) via the accessibility of Ce(III, IV) oxidation states [19]. However, it is not clear a priori whether this host will be stable toward conversion to barium carbonate ($BaCO_3$) during CO conversion. In this contribution, we compare the bulk and surface compositions of the oxidized and reduced forms of the Pd-doped perovskite materials, as well as their reactivity in CO oxidation. We also use first-principles density functional theory (DFT) to elucidate how the presence of ionic Pd in the perovskite lattice affects the location and stability of oxygen vacancies.

2. Experimental

2.1. Catalyst synthesis

Samples of $BaCe_{1-x}Pd_xO_{3-\delta}$ ($x = 0.00$, 0.05, 0.10) were prepared by grinding together BaO_2 (99%, Cerac), CeO_2 (99.9%, Cerac), and PdO (99.95%, Cerac) in appropriate stoichiometric ratios, pelletizing the ground powders, and heating them in flowing oxygen at 1000 °C for 10 h. (BaO_2 was chosen as the Ba source because it is less hygroscopic than BaO and more easily decomposed than $BaCO_3$.) The pellets were then reground, pelletized, and heated for another 10 h at 1000 °C in flowing oxygen. These samples are called "as-prepared." Reduction of as-prepared samples was carried out in flowing 5% H_2 in N_2 at 1000 °C for 1 h. Reoxidation of the reduced samples was carried out in flowing O_2 at 1000 °C for 1 h.

2.2. Bulk and surface characterization

Powder X-ray diffraction data were acquired at room temperature on a Philips XPERT MPD X-ray diffractometer, using CuK_α radiation. X-ray profiles were subjected to Rietveld analysis using the XND Rietveld code [20]. Surface areas were measured on a Micromeritics TriStar 3000 BET Analyzer. N_2 was used as the analysis gas, and liquid N_2 was used as the cryogen. Powder samples were dried and degassed by heating gently to 90 °C for 1 h, then at 200 °C for 3 h under flowing N_2 before measurement. The free space in each sample tube was determined with He, which was assumed to not adsorb. Magnetization as a function of the applied magnetic field was measured at 300 K and for fields from 0 to 1 T using a Quantum Design MPMS 5XL magnetometer.

X-ray photoelectron spectra were obtained on a Kratos Axis Ultra spectrometer with a flood of monochromatic X-rays (beam spot, 300 × 700 nm) from an AlK_α source ($E = 1486$ eV). Samples were mounted on a stainless steel sample holder using double-sided carbon tabs. The residual pressure inside the analysis chamber was $<1 \times 10^{-9}$ Torr. Survey spectra were acquired using an analyzer pass energy of 160 eV. Quantitative analysis was performed using Scofield's photoionization cross-sections [21]. High-resolution spectra in the Pd 3*d* region were acquired at a pass energy of 40 eV. Binding energies were measured with a precision of ±0.2 eV. The C 1*s* peak from adventitious carbon, at 284.8 eV, was used to correct for sample charging effects. Two standards were used for XPS analysis: Pd/γ-Al_2O_3 (5.0 wt% Pd; mean particle size, 17 nm; Fisher Scientific) and PdO/γ-Al_2O_3 (2.0 wt% Pd; mean Pd particle size, 7 nm). The PdO standard was prepared by wet impregnation of γ-alumina (HTA 102; 78 $m^2\,g^{-1}$) with $Pd(NO_3)_2$, followed by calcination in air at 600 °C for 4 h. Particle sizes were estimated from XRD line widths by applying Scherrer's equation. The binding energies obtained for the standards (Pd: 335.4, 340.5 eV; PdO: 336.7, 342.0 eV) agree with values reported in the literature [22]. In all spectra, peak-fitting of Pd(0) 3*d* doublets was constrained in the ranges 335.6–335.0 and 341.0–339.5 eV, whereas peak fitting of Pd(II) 3*d* doublets was constrained in the ranges 338.5–335.0 and 343.0–339.5 eV.

CO chemisorption experiments were carried out at atmospheric pressure using a Micromeritics AutoChem 2910. Measurements were made on 180-mg samples of the Pd-doped perovskites, after reduction, in a pulse-flow system equipped with a thermal conductivity detector. Pulses of 10% CO/He (volume 0.1638 mL) were introduced at 40 °C and 4-min intervals. Fast and total OSC were measured in a 400-mL batch reactor containing 50 mg of catalyst evacuated at room temperature for 3 h, then charged with 22 Torr CO (100%). The CO_2 yield was monitored by in situ IR spectroscopy as a function of time while the catalyst was held at either 20 or 50 °C. The temperature-dependent total OSC was evaluated by raising the temperature of the catalyst in intervals from room temperature to 300 °C. At each temperature, the reactor was allowed to equilibrate for 30 min before the IR spectrum was recorded. The $\nu_{as}(CO_2)$ rovibrational manifold was integrated over the interval 2415–2250 cm^{-1} using Kaleidagraph 4.03 (Synergy software). Peak areas were calibrated using a certified standard gas mixture, 1000 ppm CO_2(g) in N_2 (Praxair).

2.3. Assessment of catalytic activity

Temperature-programmed reaction (light-off) experiments were carried out in a fixed-bed reactor consisting of standard

glass tubing (30 mm o.d. × 20 cm) wrapped with heating tape for temperature control between room temperature and 450 °C, and two unheated glass side arms for gas inlet and outlet (8 mm o.d. × 30 cm). Each perovskite catalyst sample (100 ± 5 mg) or PdO/Al_2O_3 (45 mg) was pressed into a self-supporting pellet (16 mm diameter) and mounted at the center of the reactor. The temperature of the reacting gases was monitored by a thermocouple positioned inside the reactor, close to the catalyst pellet. Before each experiment, the catalyst was treated in flowing N_2 (60 $cm^3\ min^{-1}$) at 350 °C for 3 h to remove adsorbed moisture. The oxidation of CO was studied under steady-state conditions, using a certified gas mixture of 1000 ppm CO and 10% O_2 in N_2 (Praxair), at a constant flow rate of 50 $cm^3\ min^{-1}$ (measured at room temperature).

Outlet gases were fed to a gas-phase IR cell for on-line reaction product analysis. FTIR spectra were recorded with a Shimadzu IRPrestige-21 spectrometer, accumulating 32 scans at a resolution of 2 cm^{-1}. The spectrometer sample compartment was purged with dry, CO_2-free air from a Balston purge gas generator, and a background spectrum was subtracted from each sample spectrum to remove residual peaks. Light-off profiles were constructed by quantitative analysis of the IR spectrum of CO_2(g), as described above.

2.4. Computational methods

A plane-wave pseudopotential DFT program [23–26] was used for quantum-mechanical modeling of $BaCeO_3$, PdO, $BaCe_{0.875}Pd_{0.125}O_3$, and $BaCe_{0.875}Pd_{0.125}O_{2.875}$. The generalized gradient approximation (GGA) exchange correlation functional [27] and a 4 × 4 × 4 Monkhorst–Pack k-point sampling of the Brillouin zone [28] were used in all calculations. Atoms were represented by norm-conserving optimized [29] designed nonlocal [30] pseudopotentials. The pseudopotentials were generated with the OPIUM code [31]. Calculations were performed with a plane wave cutoff of 50 Ry.

$BaCeO_3$ and $BaCe_{0.875}Pd_{0.125}O_3$ were modeled using 40-atom 2 × 2 × 2 supercells with periodic boundary conditions, allowing for the three-dimensional octahedral tilts that were observed experimentally [18]. These supercells were relaxed both structurally and electronically, including lattice parameters and internal structural coordinates. In addition, two supercells of composition $BaCe_{0.875}Pd_{0.125}O_{2.875}$ were studied, to examine oxygen vacancy behavior. In one structure, the oxygen vacancy is next to Pd, whereas in the other, the oxygen vacancy is adjacent to two Ce atoms. Calculations on these structures used the lattice constants $a = 8.80$, $b = 8.76$, and $c = 8.82$ Å. Internal coordinates were fully relaxed.

The computational results were analyzed in three ways. DFT total energy differences were used to assess the relative thermodynamic stability of different structures. Cation–oxygen distances were used to assess oxidation states. The electronic bands at all k-points were projected (within 1 Å spheres around each atom) against an atomic orbital basis set, to construct the orbital-projected densities of states (PDOS) and identify significant changes in electronic structure.

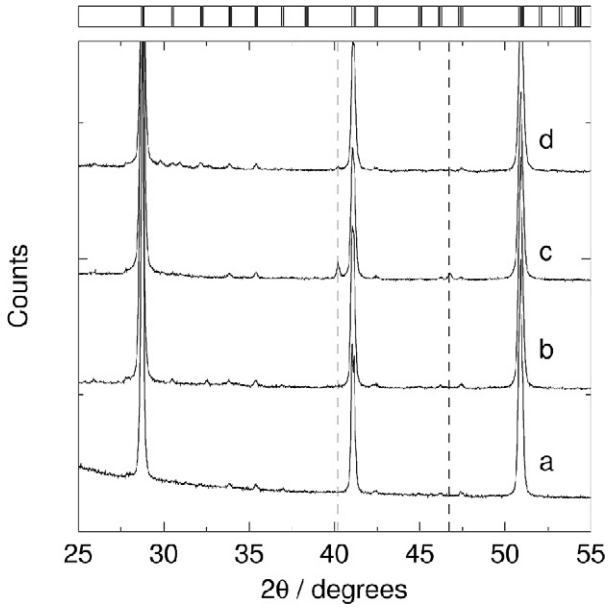

Fig. 1. XRD patterns for: (a) $BaCeO_3$; (b) $BaCe_{0.90}Pd_{0.10}O_{3-\delta}$ (as-prepared); (c) $BaCe_{0.90}Pd_{0.10}O_{3-\delta}$ (reduced); and (d) $BaCe_{0.90}Pd_{0.10}O_{3-\delta}$ (reoxidized). The vertical bars in the top frame mark expected peak positions for the perovskite phase. Dashed lines indicate peaks attributed to *fcc*-Pd.

3. Results and discussion

3.1. Bulk structures and phase compositions

The structures of the Pd-doped perovskites $BaCe_{1-x}Pd_xO_{3-\delta}$ were investigated in both their oxidized and reduced forms with $x = 0.05$ and 0.10 (corresponding to 1.7 and 3.3 wt% Pd, respectively). The XRD patterns for $BaCe_{0.90}Pd_{0.10}O_{3-\delta}$ and undoped $BaCeO_3$ are compared in Fig. 1. Peaks due to the $BaCeO_3$ perovskite structure are clearly visible in each pattern. No diffraction peaks due to CeO_2 crystallites are present, nor does the XRD pattern of the as-prepared $BaCe_{0.90}Pd_{0.10}O_{3-\delta}$ sample show any evidence for the presence of metallic Pd (Fig. 1b). After reduction in 5% H_2 for 1 h at 1000 °C, peaks consistent with the presence of *fcc*-Pd (estimated particle size 80 nm) are visible in the XRD pattern (Fig. 1c). They disappear on reoxidation for 1 h in O_2 at 1000 °C (Fig. 1d), suggesting that the metallic Pd is reabsorbed into the perovskite lattice. The BET surface area of the $BaCe_{0.90}Pd_{0.10}O_{3-\delta}$, sample (1.0 $m^2\ g^{-1}$) is essentially the same as that of undoped $BaCeO_3$ (1.1 $m^2\ g^{-1}$). Similar XRD and BET results were obtained for $BaCe_{0.95}Pd_{0.05}O_{3-\delta}$.

Rietveld refinements of the XRD patterns for as-prepared samples of $BaCe_{0.90}Pd_{0.10}O_{3-\delta}$ were performed before and after reduction. Fig. 2a shows single-phase fitting of the orthorhombic perovskite before reduction within the *Pnma* space group. Refinement of space occupancy confirmed that 90% of the palladium was incorporated into the B-site of the perovskite lattice, consistent with our previous report of Rietveld refinement on neutron powder diffraction data [18]. The oxygen occupancy was also refined, and gave one oxygen vacancy per Pd atom. Fig. 2b shows the fit for $BaCe_{0.90}Pd_{0.10}O_{3-\delta}$ after reduction. Contributions from both the orthorhombic *Pnma* per-

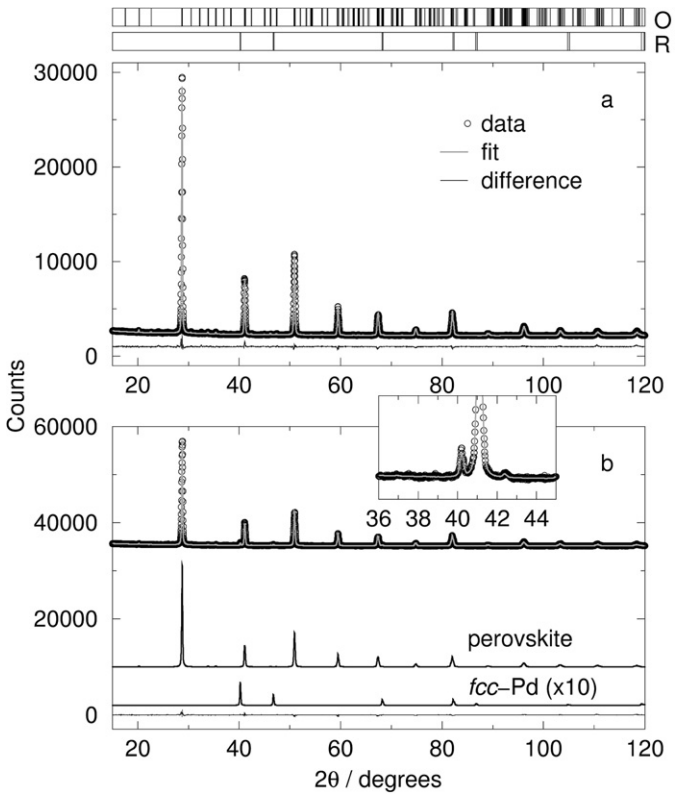

Fig. 2. Rietveld refinement of XRD patterns for $BaCe_{0.90}Pd_{0.10}O_{3-\delta}$: (a) as-prepared sample, showing data (points), the single-phase Rietveld fit to the perovskite structure with 10% Pd on the Ce site, and the difference profile; (b) reduced sample, showing data (points), the two-phase Rietveld fit and the difference profile, as well as the individual contributions to the profile from the perovskite and from *fcc*-Pd. For clarity, the latter has been scaled ten-fold. The inset shows the main *fcc*-Pd peak in an expanded view. The vertical bars in the top frame mark expected peak positions for perovskite (O) and *fcc*-Pd (R).

ovskite phase and *fcc*-Pd are evident. Their relative amounts are $(91 \pm 1)\%$ and $(9 \pm 1)\%$, respectively, consistent with quantitative extrusion of palladium from the perovskite host.

3.2. Surface analyses

The surface composition of $BaCe_xPd_{1-x}O_{3-\delta}$ was investigated by XPS. A representative survey scan is shown in Fig. 3. Quantitative analysis reveals that the surfaces of both as-prepared samples ($x = 0.05$, 0.10) contain Ba, Ce, and Pd in roughly the same proportions as the bulk (within the accepted error of the technique); see Table 1. This result contrasts with a recent report that no Pd 3*d* signals were detectable for $LaFe_{0.77}Co_{0.17}Pd_{0.06}O_3$ [9]. On reduction, both $BaCe_xPd_{1-x}O_{3-\delta}$ samples exhibit a dramatic decrease in the near-surface concentration of Pd. On reoxidation, Pd reappears at the perovskite surface. These changes are illustrated by the dramatic intensity fluctuations in the high-resolution XPS scans of the Pd 3*d* region (Figs. 4 and 5).

The Pd 3*d* peaks are deconvoluted into pairs of spin–orbit doublets for the as-prepared samples in Figs. 4a and 5a. The signals due to cationic palladium appear at 337.7 and 342.9 eV. These binding energies are blue-shifted by ca. 1.0 eV with respect the Pd 3*d* binding energies in PdO [32]. This behavior

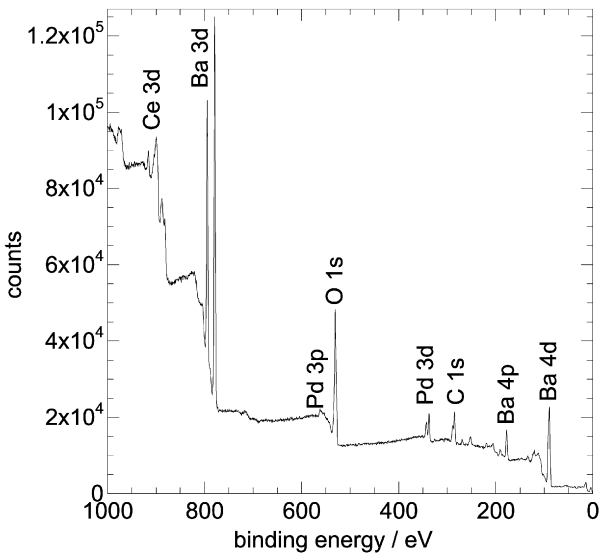

Fig. 3. XPS survey scan for $BaCe_{0.90}Pd_{0.10}O_{3-\delta}$ (as-prepared).

Table 1
Apparent surface compositions[a] and Pd 3*d* binding energies, in Pd-containing materials

Sample	At%			Binding energies (eV)	
	Ba	Ce	Pd	Pd(II)	Pd(0)
$Pd/\gamma\text{-}Al_2O_3$					335.4, 340.5
$PdO/\gamma\text{-}Al_2O_3$				336.7, 342.0	
$BaCeO_3$	54	46	–		
$BaCe_{0.95}Pd_{0.05}O_{3-\delta}$					
As-prepared	54	39	7.5	337.5, 342.7	n.d.
Reduced	70	29	1.3	n.d.	335.4, 340.4
$BaCe_{0.90}Pd_{0.10}O_{3-\delta}$					
As-prepared	59	31	10	337.7, 342.9	335.5, 339.9
Reduced	65	34	1.4	337.7, 342.0	335.2, 340.3
Reoxidized	63	34	3.0	337.5, 342.8	335.6, 339.3
After CO oxidation	59	35	6.4	337.7, 342.9	335.8, 339.9

[a] Uncorrected for differing escape depths of photoelectrons from different elements.

is expected for the more highly ionic environment of Pd(II) in the perovskite host compared with PdO and is consistent with its proposed location at the B site of the perovskite lattice. Similar shifts in binding energy were reported for commercial three-way catalysts containing Pd and CeO_2 [33], for highly dispersed Pd/Al_2O_3 [34], and for a $Ce_{1-x}Pd_xO_{2-\delta}$ "solid solution" synthesized by a combustion method [22], but not for nanoparticles of PdO dispersed on SiO_2 [35]. In these cases, the shifts have been interpreted as evidence of an intimate interaction between Pd(II) and the support.

Higher binding energies for cationic Pd were also reported in the XPS and the Pd K-edge positions for Pd-doped La(Fe,Co)O_3 [6,8,16]. In these systems, the shifts as well as the EXAFS curve fits were interpreted as evidence of the incorporation of the noble metal in the perovskite matrix as six-coordinate Pd(III) [6–8]. More information about the Pd oxidation state in as-prepared $BaCe_{0.95}Pd_{0.05}O_{3-\delta}$ was sought by investigating its magnetic susceptibility. Both this material and $BaCeO_3$ are diamagnetic, as shown by the inverse dependence

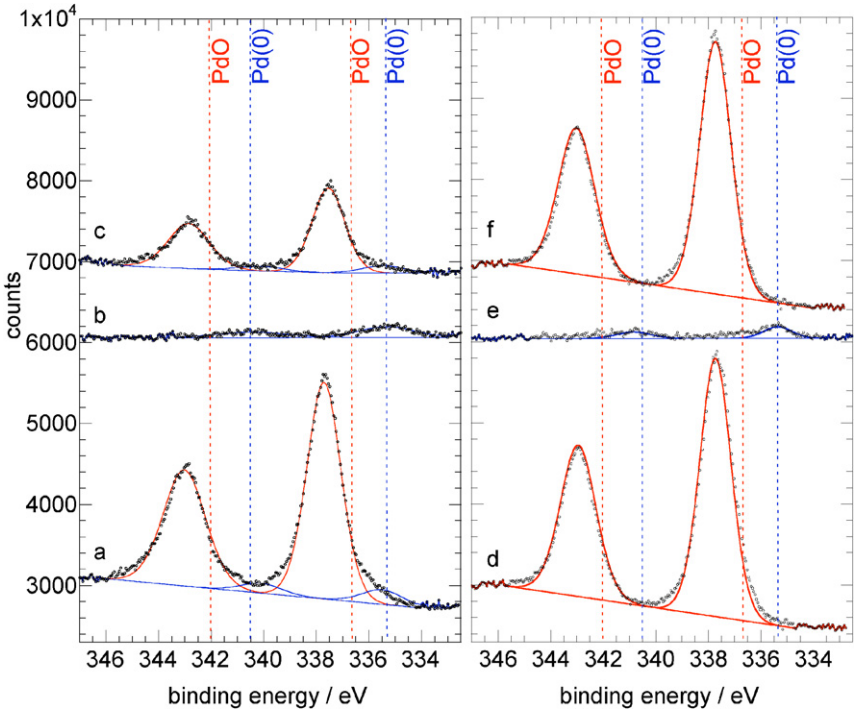

Fig. 4. High-resolution XPS scans in Pd 3*d* region for $BaCe_{0.90}Pd_{0.10}O_{3-\delta}$, before (a, b, c) and after (d, e, f) their use as CO oxidation catalysts: (a, d) as-prepared samples; (b, e) reduced samples; (c, f) reoxidized samples. Spectra are vertically offset but plotted on the same vertical scale in order to compare intensities. Dashed lines indicate the expected peak positions of the Pd spin–orbit doublets ($3d_{5/2}$, $3d_{3/2}$) for nanoparticulate Pd(0) (blue) and nanoparticulate PdO (red). (For interpretation of the references to color in this figure legend, the reader is referred to the web version of this article.)

of the magnetization on the magnetic field (Fig. 6). This result confirms that Pd is not associated with unpaired electrons; the magnetic susceptibility is significantly lower than values observed for materials in which Pd has an unpaired electron [36]. Therefore, we suggest that the most likely Pd oxidation state assignment for $BaCe_{1-x}Pd_xO_{3-\delta}$ is Pd(II). This conclusion is further supported by our computational investigation of its electronic structure (see below).

The XPS of as-prepared $BaCe_{0.90}Pd_{0.10}O_{3-\delta}$ contains a very weak doublet with chemical shifts characteristic of metallic palladium. Quantitative analysis of the XPS spectrum shows that ca. 8% of the palladium in the sample is present in the Pd(0) form, consistent with the results of X-ray Rietveld refinement for the bulk material (see above). The XPS spectrum of the as-prepared material with $x = 0.05$ shows no sign of Pd(0) (Fig. 5d), confirming that essentially all of its Pd is present in cationic form.

On reduction of as-prepared $BaCe_{0.90}Pd_{0.10}O_{3-\delta}$ in 5% H_2 at 1000 °C, the XPS signals due to cationic Pd are completely suppressed (Fig. 4b), yet the signals due to Pd(0) are not appreciably more intense. Nevertheless, Rietveld analysis of the XRD pattern for the reduced sample confirms that virtually all of the Pd in the sample is present in metallic form (see above). The same changes were observed for $BaCe_{0.95}Pd_{0.05}O_{3-\delta}$ (Fig. 5b). XPS spectra were recorded as a function of reduction temperature, shown in the region of the Pd 3*d* peaks in Fig. 7. Although the Pd(0) signal intensity initially increases, it decreases abruptly above 300 °C. Previously, XRD results indicated expansion of the perovskite cell volume due to extrusion of Pd at 200 °C, although diffraction peaks for *fcc*-Pd are barely detectable by XRD below 300 °C [18]. They appear prominently starting at 400 °C. These results demonstrate the increasing particle size of metallic Pd, estimated by XRD line broadening to ca. 12 nm at 300 °C and 45 nm at 400 °C, with increasing reduction temperature. However, grain growth cannot be entirely responsible for the suppression of the XPS signal in the fully reduced material, because the much more intense Pd(II) signal of as-prepared $BaCe_{0.90}Pd_{0.10}O_{3-\delta}$ arises from a material with much larger grains (BET surface area 1.0 $m^2\,g^{-1}$). Instead, the signal suppression is a likely consequence of the previously reported tendency of $BaCeO_3$ to regrow over elemental Pd [18].

We were unable to detect CO chemisorption on reduced $BaCe_xPd_{1-x}O_{3-\delta}$; thus, the "accessible" Pd(0) content is <0.1% of the total Pd. Reduction also causes the surface to become enriched in Ba (see Table 1). This is consistent with extrusion of the excess A-site cation, possibly as $Ba(OH)_2$ (amorphous, not detected by XRD) on removal of Pd from the perovskite. A similar explanation was advanced for $LaMn_{0.976}Rh_{0.024}O_{3+\delta}$ after its reduction in CO. The XPS spectrum showed higher-than-expected amounts of La, C, and O on the surface, attributed to the presence of surface lanthanum carbonates and oxycarbonates [5].

Reoxidation of highly reduced $BaCe_xPd_{1-x}O_{3-\delta}$ in flowing O_2 for 1 h at 1000 °C resulted in the reappearance of signals corresponding to cationic Pd (Figs. 4c and 5c). The peak positions confirm that the metal is reabsorbed as Pd(II) into the B sites of the perovskite lattice, consistent with the reversible

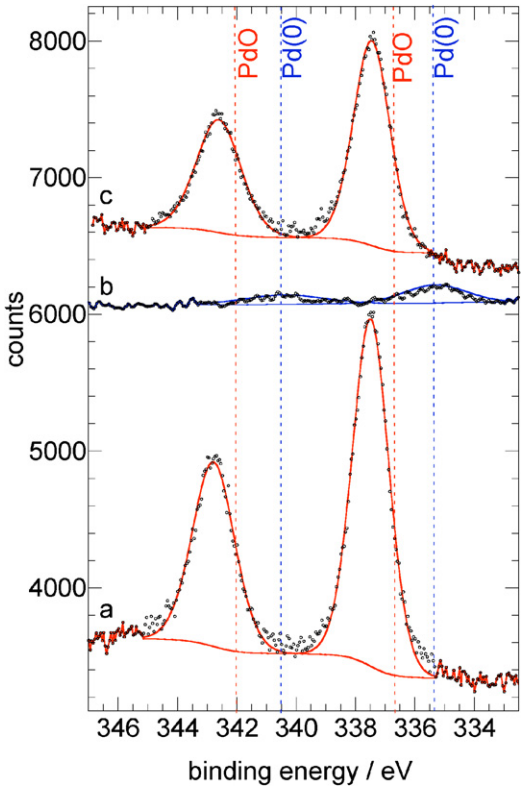

Fig. 5. High-resolution XPS scans in Pd 3*d* region for $BaCe_{0.95}Pd_{0.05}O_{3-\delta}$: (a) as-prepared; (b) reduced; and (c) reoxidized. Spectra are vertically offset but plotted on the same vertical scale in order to compare intensities. Dashed lines indicate the expected peak positions of the Pd spin–orbit doublets ($3d_{5/2}$, $3d_{3/2}$) for nanoparticulate Pd(0) (blue) and nanoparticulate PdO (red). (For interpretation of the references to color in this figure legend, the reader is referred to the web version of this article.)

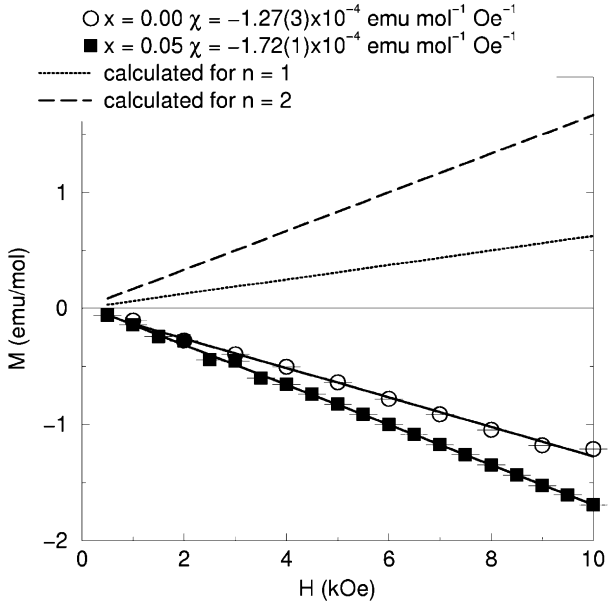

Fig. 6. Magnetization at 300 K as a function of magnetic field for $BaCe_{1-x}Pd_xO_{3-\delta}$, with $x = 0.00$ and $x = 0.05$. Values of the measured susceptibility χ are indicated; no diamagnetic corrections were made. Lines with positive slopes were calculated for $x = 0.05$, assuming $n = 1$ and $n = 2$ unpaired electrons.

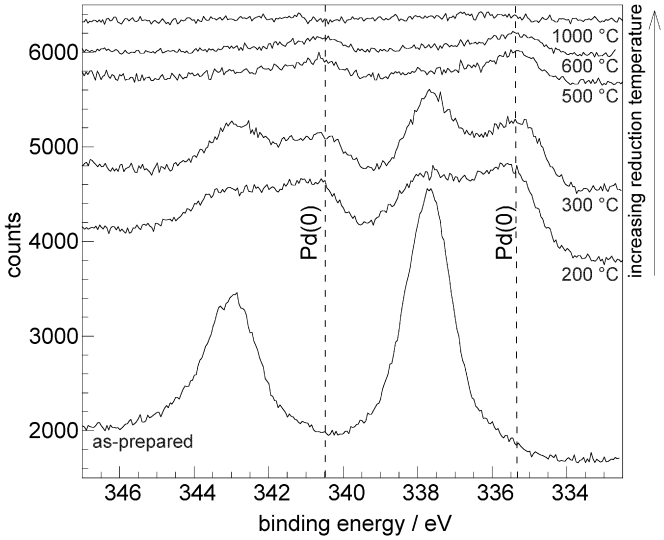

Fig. 7. High-resolution XPS scans in Pd 3*d* region for $BaCe_{0.95}Pd_{0.05}O_{3-\delta}$, as-prepared, and reduced in 5% H_2 for 1 h at each one of the temperatures indicated. Spectra are vertically offset but plotted on the same vertical scale in order to compare intensities. Dashed lines indicate the expected peak positions of the Pd spin–orbit doublet ($3d_{5/2}$, $3d_{3/2}$) for nanoparticulate Pd(0).

change in cell volume observed by time-of-flight neutron diffraction and XRD during redox cycling [18]. However, the signals for cationic Pd in samples reoxidized for just 1 h are less intense than those in the as-prepared samples, confirming our previous finding that Pd incorporation into the perovskite structure is considerably less rapid than its extrusion [18]. Expansion of the perovskite cell volume indicates egress of Pd(II) from the lattice starting at 200 °C, however, little reincorporation of the extruded Pd(0) was observed below 600 °C. The large Pd(0) particle size, the slow kinetics of oxidation of Pd(0), and the need to incorporate additional A-site cations all likely contribute to the greater difficulty of Pd ingress into the perovskite host.

3.3. Evaluation of light-off behaviors

Catalytic CO oxidation was studied in a flow of 1000 ppm CO with 10% (excess) O_2 (balance N_2, at atmospheric pressure), chosen to mimic the oxidizing conditions in the exhaust gas of lean-burn diesel engines (redox stoichiometry $S = 200$). The light-off curves for 100-mg samples of as-prepared, reduced, and reoxidized $BaCe_{0.90}Pd_{0.10}O_{3-\delta}$ are superimposed in Fig. 8. The highest activity is associated with as-prepared $BaCe_{0.90}Pd_{0.10}O_{3-\delta}$, for which $T_{50} = 83$ °C, compared with 165 °C for the fully reduced material. The as-prepared material also shows significantly higher conversion than the reduced material at 200 °C (92 vs 80%). A similar result was reported for a family of catalysts prepared by depositing noble metal oxides (including PdO) onto perovskite supports (including $BaCeO_3$, $SrCeO_3$, $SrZrO_3$, and $SrTiO_3$); their activity for the oxidation of CO by NO declined when essentially all of the noble metal oxide was reduced to metallic form [37]. The catalytic activity of 45 mg PdO/Al_2O_3 (2.0 wt% Pd), measured under the same reaction conditions, is shown in Fig. 9 (inset); its T_{50} is al-

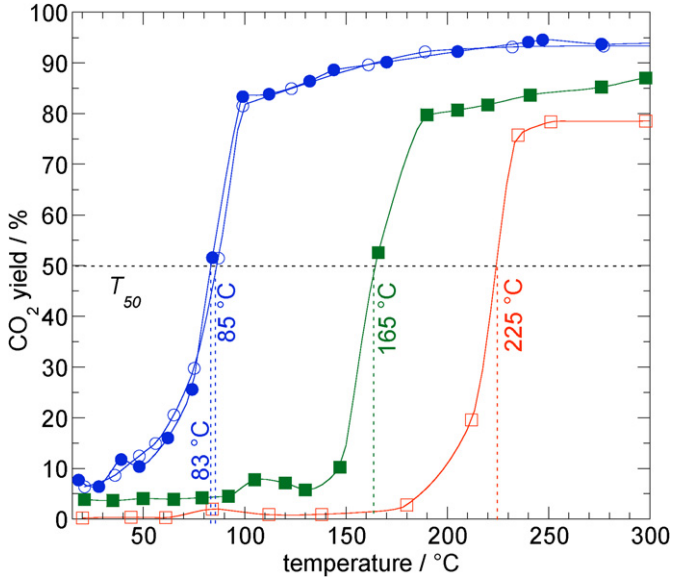

Fig. 8. Temperature-programmed reaction profiles for the oxidation of CO (1000 ppm) by excess O_2 (10% in N_2, total flow rate 50 $cm^3\ min^{-1}$) over 100 mg $BaCe_{0.90}Pd_{0.10}O_{3-\delta}$: as-prepared (solid blue circles), reduced (solid green squares), and reoxidized forms (open blue circles), as well as $BaCeO_3$ (open red squares). Lines are drawn only to guide the eye. (For interpretation of the references to color in this figure legend, the reader is referred to the web version of this article.)

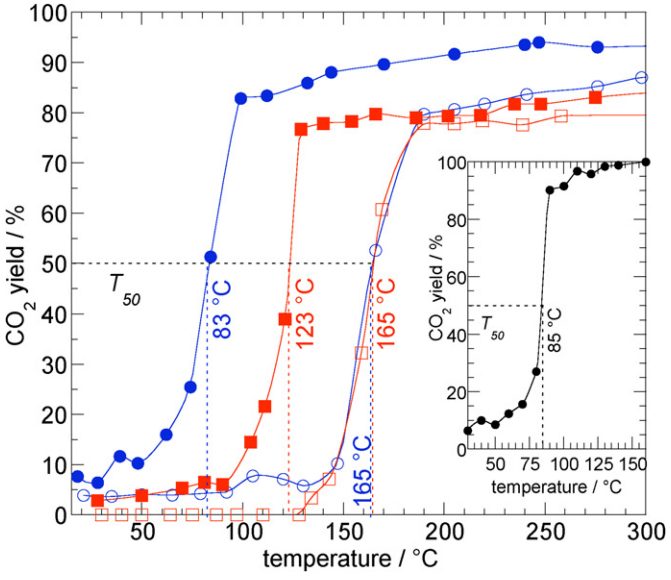

Fig. 9. Comparison of temperature-programmed reaction profiles for the oxidation of CO (1000 ppm) by excess O_2 (10% in N_2, total flow rate 50 $cm^3\ min^{-1}$) over 100 mg $BaCe_{0.90}Pd_{0.10}O_{3-\delta}$, as-prepared (solid blue circles) and reduced (open blue circles), and over $BaCe_{0.95}Pd_{0.05}O_{3-\delta}$, as-prepared (solid red squares) and reduced (open red squares). The inset shows the profile for 45 mg PdO/Al_2O_3 (2.0 wt% Pd, black) measured under the same conditions. Lines are drawn only to guide the eye. (For interpretation of the references to color in this figure legend, the reader is referred to the web version of this article.)

most identical to that of the fully oxidized $BaCe_{0.90}Pd_{0.10}O_{3-\delta}$. The CO oxidation activity of 100 mg of undoped $BaCeO_3$ was also measured for comparison, because many perovskites are themselves catalysts for CO oxidation due to the presence of structural defects such as cation and anion vacancies [4]. Its light-off temperature is $T_{50} = 225\,°C$.

The XRD pattern of the as-prepared doped perovskite (Fig. 10) remains essentially unchanged after the reaction with CO, with no signals visible for a $BaCO_3$ phase. Thus it appears that the $BaCeO_3$ structure is stable under these reaction conditions, which extended up to 400 °C and over 40 h on stream. Reoxidation of the reduced material completely restored its low-temperature activity, with $T_{50} = 85\,°C$, Fig. 8. The effect of Pd loading is shown in Fig. 9. On decreasing the amount of Pd dopant from $x = 0.10$ to $x = 0.05$ (i.e., from 3.3 to 1.7 wt% Pd), the activity decreased, as reflected by a 40 °C increase in the light-off temperature, T_{50}.

This effect is seen only for the oxidized samples. The light-off temperatures of the reduced samples are virtually identical (165 °C) for the different Pd loadings, Fig. 9, arguing against a significant role for metallic palladium in the CO oxidation reaction in this temperature range. XRD line-broadening analysis is unable to provide accurate grain sizes for the Pd(0) particles, nor could these grain sizes be determined by microscopy [18]. However, the XPS and CO chemisorption results suggest that Pd(0) is largely inaccessible [i.e., covered with $BaCeO_3$ and/or $Ba(OH)_2$)] and thus cannot contribute to the reactivity. The residual activity of the reduced catalysts may be attributed to traces of Pd(II) remaining in the perovskite host.

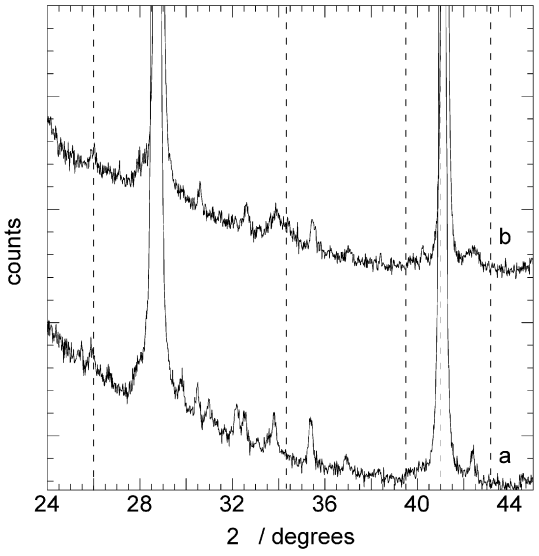

Fig. 10. XRD patterns for as-prepared $BaCe_{0.90}Pd_{0.10}O_{3-\delta}$, (a) before; and (b) after its use as a catalyst for CO oxidation ($T_{max} = 400\,°C$). The dashed lines indicate expected peak positions for $BaCO_3$.

3.4. Chemical state of Pd after reaction

XPS analysis was repeated on samples of $BaCe_{0.90}Pd_{0.10}O_{3-\delta}$ after their use as CO oxidation catalysts (40 h on stream, $30 \leqslant T \leqslant 400\,°C$). The results are shown in Figs. 4d–4f, on the same intensity scale as the XPS scans of the fresh samples. The intensities of the peaks assigned to cationic Pd changed only slightly for the as-prepared sample after reac-

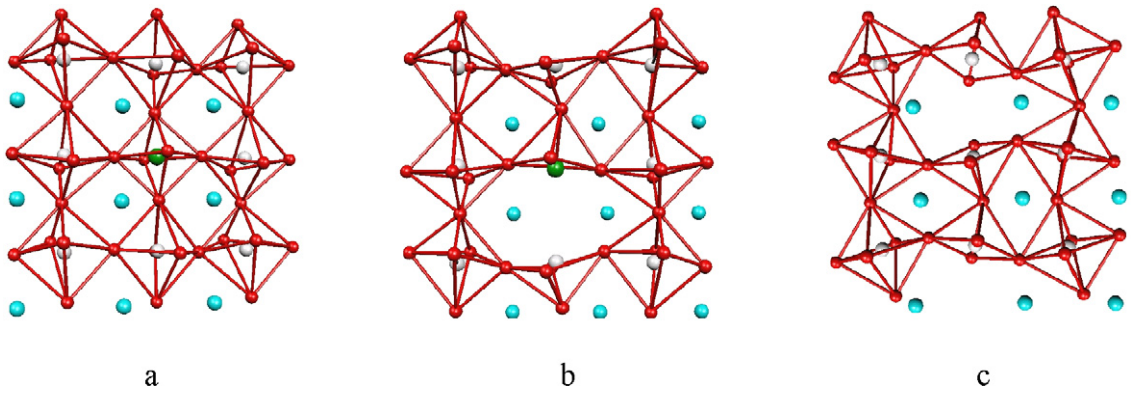

Fig. 11. Theoretically-computed structures of (a) $BaCe_{0.875}Pd_{0.125}O_3$; (b) $BaCe_{0.875}Pd_{0.125}O_{2.875}$, with a vacancy between Ce and Pd; and (c) $BaCe_{0.875}Pd_{0.125}O_{2.875}$, with a vacancy between two Ce sites (layer containing Pd not shown). Color scheme: Ba (blue), Ce (white), Pd (green), O (red). (For interpretation of the references to color in this figure legend, the reader is referred to the web version of this article.)

tion, as was expected because this material was already highly oxidized and had similar surface and bulk Pd concentrations. The XPS intensity of the reduced sample also changed little, consistent with the fact that most of the Pd(0) remained below the surface layers probed by XPS. However, the intensity of the cationic Pd signals for the reoxidized sample increased significantly. Because the XRD pattern confirms that Pd is fully incorporated in the perovskite matrix for this sample [18], the XPS result implies that cationic Pd can migrate toward the surface under relatively mild reaction conditions ($\leqslant$400 °C).

3.5. Effect of Pd-doping on oxygen vacancies

Our light-off curves show that for low-temperature (<200 °C) CO oxidation by Pd-doped $BaCeO_3$ perovskite catalysts, the presence of cationic Pd is associated with superior activity relative to perovskite-supported metallic Pd, which is inaccessible to the reactants. This finding suggests that the doped perovskite itself is the catalyst. The activity at T_{50} = 85 °C of as-prepared, low-surface area $BaCe_{0.90}Pd_{0.10}O_{3-\delta}$ (1.0 $m^2\,g^{-1}$) corresponds to a turnover frequency of 5.5 × 10^2 mol CO (mol Pd)$^{-1}$ s^{-1}, compared with 2.8 × 10^3 mol CO (mol Pd)$^{-1}$ s^{-1} for a conventionally formulated PdO/γ-Al_2O_3 catalyst (2 wt% Pd, 7 nm average particle size) at the same temperature under the same reaction conditions. The origin of the high reactivity in such a low-surface area material is under investigation, although some insight has already been gained from theoretical analysis of the oxygen vacancies in these materials.

The influence of the Pd dopant on vacancy stability was investigated using DFT. The total energy of $BaCe_{0.875}Pd_{0.125}O_{2.875}$, with an oxygen vacancy between Pd and Ce, was 0.95 eV lower than the same composition with a vacancy between two Ce sites. We attribute this energy difference to the relative ease of forming and accommodating a square-planar Pd(II) compared with two much larger Ce(III) cations. The energy difference for vacancy formation was further investigated by analysis of the relaxed DFT structures. In $BaCe_{0.875}Pd_{0.125}O_3$ (no oxygen vacancy), the Pd and Ce cations each had six O neighbors (Fig. 11a), with Pd–O and Ce–O interatomic distances of (2.02 ± 0.01) and (2.26 ± 0.02) Å, respectively. These distances are consistent with the oxidation states Pd(IV) and Ce(IV), because the expected ionic radii for sixfold coordination are $R_{Pd(IV)} = 0.615$, $R_{Ce(IV)} = 0.87$, and $R_{O^{2-}} = 1.40$ Å [38,39]. When an oxygen vacancy was introduced between Pd and Ce (Fig. 11b), four of the Pd–O bonds expanded slightly to 2.04 Å, and the fifth bond was essentially broken (2.66 Å). These bond lengths are characteristic of square-planar Pd(II) (typically, $R_{Pd(II)} = 0.64$ Å in this geometry [38,39]). The Ce cation adjacent to the vacancy had four bonds to oxygen that contracted slightly, to (2.22 ± 0.02) Å, while the fifth bond shrank significantly, to 2.05 Å. In other words, Ce(IV) compensated for the loss of one bond to oxygen by strengthening all others, thereby maintaining its maximum oxidation state. When the vacancy occurred instead between two Ce(III) ions (Fig. 11c), the Ce–O bond lengths did not change significantly. We attribute this result to compensating effects; whereas an octahedral Ce(III) would desire longer bonds, the fivefold coordination favors bond shortening.

The electronic PDOS for the Pd 4*d* states supports our assessment of bonding around Pd in the perovskite. In Fig. 12a, the Pd PDOS in PdO is shown as a reference, with 0 eV representing the top of the valence band (Fermi energy). Fig. 12b shows the PDOS for Pd in $BaCe_{0.875}Pd_{0.125}O_{2.875}$ with a vacancy adjacent to Pd. The individual peaks and the total bandwidth for the perovskite are narrower than in PdO, supporting our experimental XPS finding that the Pd(II) environment in $BaCe_{1-x}Pd_xO_{3-\delta}$ is more ionic than in PdO. The integrated 4*d*-state occupancies in Figs. 12a and 12b are identical, consistent with our identification of the Pd oxidation state as (II) when the vacancy is adjacent to Pd. An intense, localized peak just below the Fermi energy is due to the d_{z^2} orbital, occupied and unbonded in the square-planar environment. For comparison, the PDOS for $BaCe_{0.875}Pd_{0.125}O_{2.875}$ with a six-coordinate Pd cation is shown in Fig. 12c. The integrated occupancy is lower, and the filled states have lower energy, indicative of Pd(IV).

3.6. Effect of oxygen vacancies on catalytic behavior

Enhanced oxygen mobility has been demonstrated in transition-metal-doped anion-conducting perovskite membranes [4]

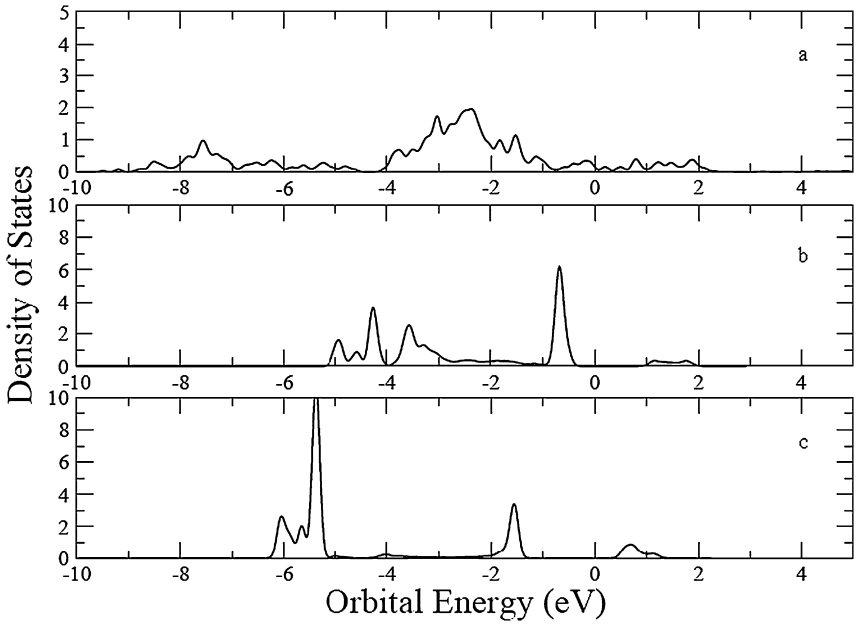

Fig. 12. Theoretically-computed projected densities of states onto Pd 4*d* orbitals, for (a) PdO; (b) $BaCe_{0.875}Pd_{0.125}O_{2.875}$, with a vacancy between Ce and Pd; and (c) $BaCe_{0.875}Pd_{0.125}O_{2.875}$, with a vacancy between two Ce sites.

and has been correlated with activity in oxidation of CO by perovskite catalysts as well as CeO_2–ZrO_2 automotive catalysts [40,41]. As the amount of cationic Pd in $BaCe_{1-x}Pd_xO_{3-\delta}$ increases, the mobility of lattice oxygen should increase due to the larger number of oxygen vacancies [3]. The detailed mechanism of mobility in the doped perovskites has been proposed to involve rapid diffusion at grain [42] and microdomain [43] boundaries. However, oxygen diffusion coefficients are predicted to be larger in bulk ceria than in nanocrystalline CeO_2, and precious metal doping suppresses the formation of grain boundaries when the smaller dopant cation is more easily accommodated than large Ce(III) ions in the partially reduced structure [44]. Although removal of surface oxygen from bulk oxides is more difficult than removal in their nanocrystalline counterparts, the presence of a dopant in the surface layer facilitates the release of oxygen from the bulk material. For example, Pd doping in $La_{1-x}Sr_xFe(Pd)O_{3\pm\delta}$ has been shown to increase both low-temperature oxygen mobility and catalytic activity by decreasing the reduction temperature of the perovskite [45]. The reaction mechanism may involve CO adsorption on exposed Pd(II) in the perovskite surface layer, followed by conversion to CO_2 or a surface carbonate on reaction with this labile oxygen from the perovskite host.

The availability of lattice oxygen in our Pd-doped perovskites was investigated by quantifying their ability to oxidize CO in the absence of added oxidant. The results are shown in Fig. 13. At 30-min intervals, the temperature of a batch reactor containing 50 mg of catalyst and 22 Torr CO was raised, and the CO_2 yield was measured. Undoped $BaCeO_3$ was not noticeably reduced by CO under these conditions until the temperature exceeded 160 °C. In contrast, both Pd-doped perovskites ($x = 0.05$ and 0.10) in their as-prepared (i.e., fully oxidized) states oxidized CO even at 20 °C, and the yield of CO_2 increased monotonically with temperature. The OSC was

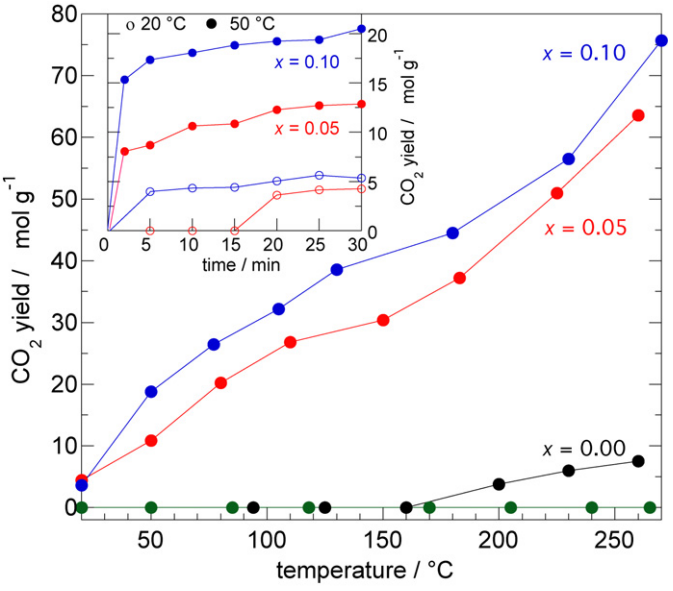

Fig. 13. Temperature-dependent oxygen storage capacity, measured as the ability to oxidize CO to CO_2 in a batch reactor in the absence of an external oxidant, for $BaCeO_3$ (black), as-prepared $BaCe_{0.90}Pd_{0.10}O_{3-\delta}$ (blue), reduced $BaCe_{0.90}Pd_{0.10}O_{3-\delta}$ (green), and as-prepared $BaCe_{0.95}Pd_{0.05}O_{3-\delta}$ (red). The inset shows the time-evolution of the CO_2 formed over as-prepared $BaCe_{0.90}Pd_{0.10}O_{3-\delta}$ (blue) and as-prepared $BaCe_{0.95}Pd_{0.05}O_{3-\delta}$ (red), at 20 (open circles) and 50 °C (filled circles). Lines are drawn only to guide the eye. (For interpretation of the references to color in this figure legend, the reader is referred to the web version of this article.)

higher for $BaCe_{0.90}Pd_{0.10}O_{3-\delta}$ than for $BaCe_{0.95}Pd_{0.05}O_{3-\delta}$ at all temperatures, reaching 76 μmol CO_2 g^{-1} of catalyst at 270 °C. Interestingly, the OSC was the same for both materials (27 μmol CO_2 g^{-1} of catalyst) at the particular temperatures corresponding to their light-off under flow conditions, 83 °C ($x = 0.10$) and 123 °C ($x = 0.05$). The OSC of $BaCe_{0.90}$-

$Pd_{0.10}O_{3-\delta}$ was completely suppressed below 300 °C when the material was prereduced in 5% H_2 to convert Pd(II) to Pd(0).

Total OSC is poorly correlated with oxidation activity under catalyst operating conditions [42]. A better indicator is the fast OSC [45]. The temporal evolution of CO_2 over the doped perovskite catalysts was evaluated at two temperatures (Fig. 13, inset). At both 20 and 50 °C, there was an initial, rapid phase of CO oxidation (<2 min) over $BaCe_{0.90}Pd_{0.10}O_{3-\delta}$, followed by much slower formation of CO_2 over the next 30 min. The fast OSC accounted for 75% of the total OSC under these conditions. Similar behavior was observed for $BaCe_{0.95}Pd_{0.05}O_{3-\delta}$ at 50 °C, although both the fast and total OSCs were lower. The fast OSC accounted for 63% of the total OSC for this material at 50 °C; no fast OSC was detected at 20 °C.

4. Conclusion

The details of incorporation of Pd as Pd(II) into the crystalline lattice of the perovskite $BaCeO_3$ have been characterized both structurally and electronically. The catalytic activity of the doped perovskite for CO oxidation in an oxidizing atmosphere appears to be maximized not by the stabilization of Pd nanoparticles or increased dispersion of PdO, but rather by the presence of cationic Pd(II) in the perovskite host. Experimentally, we found that $BaCeO_3$ can accommodate up to 10 at% Pd(II) on the B site. Reduction causes extrusion of Pd(0) from the perovskite structure in a fully reversible process. DFT results confirm the location and oxidation state of Pd(II) and predict a square-planar geometry accompanied by an adjacent oxygen vacancy. Pd doping of the perovskite appears to promote the catalytic oxidation of CO, despite the very low surface area, through increased oxygen vacancy concentration, which facilitates oxygen ion transport and thus diffusion through the bulk to the surface.

Acknowledgments

This work was funded by the National Science Foundation (Award CTS-0508455) and by the US Department of Energy, Basic Energy Sciences (Grant DE-FG02-05ER15725). This work made use of MRL Central Facilities, supported by the MRSEC Program of the National Science Foundation (Award DMR05-20020). A.M.R. acknowledges the support of the Office of Naval Research (Grants N00014-00-1-0372 and N00014-00-1-0365) and computational support from the High-Performance Computing Modernization Office of the US Department of Defense. J.W.B. acknowledges the support of a GAANN fellowship from the US Department of Education.

References

[1] W.F. Libby, Science 171 (1971) 499–500.
[2] D.B. Meadowcroft, Nature 226 (1970) 847–848.
[3] R.J.H. Voorhoeve, D.W. Johnson Jr., Science 195 (1977) 827–833.
[4] M.A. Peña, J.L.G. Fierro, Chem. Rev. 101 (2001) 1981–2017.
[5] N. Guilhaume, M. Primet, J. Catal. 165 (1997) 197–204.
[6] Y. Nishihata, J. Mizuki, T. Akao, H. Tanaka, M. Uenishi, M. Kimura, T. Okamoto, N. Hamada, Nature 418 (2002) 164–167.
[7] H. Tanaka, M. Uenishi, M. Taniguchi, I. Tan, K. Narita, M. Kimura, K. Kaneko, Y. Nishihata, J. Mizuki, Catal. Today 117 (2006) 321–328.
[8] M. Uenishi, M. Taniguchi, H. Tanaka, M. Kimura, Y. Nishihata, J. Mizuki, T. Kobayashi, Appl. Catal. B 57 (2005) 267–273.
[9] K. Zhou, H. Chen, Q. Tian, Z. Hao, D. Shen, X. Xu, J. Mol. Catal. A Chem. 189 (2002) 225–232.
[10] H. Tanaka, Catal. Surv. Asia 9 (2005) 63–73.
[11] M. Misono, Catal. Today 100 (2005) 95–100.
[12] S. Cimino, L. Lisi, R. Pirone, G. Russo, Ind. Eng. Catal. Res. 43 (2004) 6670–6679.
[13] A. Civera, G. Negro, S. Specchia, G. Saracco, V. Specchia, Catal. Today 100 (2005) 275–281.
[14] S. Specchia, A. Civera, G. Saracco, V. Specchia, Catal. Today 117 (2006) 427–432.
[15] D. Ciuparu, M.R. Lyubovksy, E. Altman, L.D. Pfefferle, A. Datye, Catal. Rev. 44 (2002) 593–649.
[16] I. Twagirashema, M. Engelmann-Pirez, M. Frere, L. Burylo, L. Gengembre, C. Dujardin, P. Granger, Catal. Today 119 (2007) 100–105.
[17] S. Cimino, G. Landi, L. Lisi, G. Russo, Catal. Today 117 (2006) 454–461.
[18] J. Li, U.G. Singh, J.W. Bennett, K. Page, J. Weaver, J.-P. Zhang, T. Proffen, A.M. Rappe, S.L. Scott, R. Seshadri, Chem. Mater. 19 (2007) 1418–1426.
[19] H.C. Yao, Y.F.Y. Yao, J. Catal. 86 (1984) 254–265.
[20] J.-F. Bérar, P. Garnier, NIST Spec. Publ. 846 (1992) 212.
[21] J.H. Scofield, J. Electron Spectrosc. Relat. Phenom. 8 (1976) 129.
[22] P.B.K.R. Priolkar, P.R. Sarode, M.S. Hegde, S. Emura, R. Kumashiro, N.P. Lalla, Chem. Mater. 14 (2002) 2120–2128.
[23] P. Hohenberg, W. Kohn, Phys. Rev. B 136 (1964) 864–871.
[24] W. Kohn, L.J. Sham, Phys. Rev. A 140 (1965) 1133–1138.
[25] G. Kresse, J. Furthmuller, Phys. Rev. B 54 (1996) 11169–11186.
[26] M.C. Payne, M.P. Teter, D.C. Allan, T.A. Arias, J.D. Joannapoulos, Rev. Mod. Phys. 64 (1992) 1045–1097.
[27] J.P. Perdew, K. Burke, M. Ernzerhof, Phys. Rev. Lett. 77 (1996) 3865–3868.
[28] H.J. Monkhorst, J.D. Pack, Phys. Rev. B 13 (1976) 5188–5192.
[29] A.M. Rappe, K.M. Rabe, E. Kaaxiras, J.D. Joannapoulos, Phys. Rev. B 41 (1990) 1227–1230.
[30] N.J. Ramer, A.M. Rappe, Phys. Rev. B 59 (1999) 12471–12478.
[31] http://opium.sourceforge.net.
[32] M. Brun, A. Berthet, J.C. Bertolini, J. Electron Spectrosc. Relat. Phenom. 104 (1999) 55–60.
[33] P.J. Schmitz, K. Otto, J.E. deVries, Appl. Catal. A 92 (1992) 59–72.
[34] K. Otto, L.P. Haack, J.E. deVries, Appl. Catal. B 1 (1992) 1–12.
[35] E.H. Voogt, A.J.M. Mens, O.L.J. Gijzeman, J.W. Geus, Surf. Sci. 350 (1996) 21–31.
[36] B.D. Cullity, Introduction to Magnetic Materials, Addison–Wesley, Reading, MA, 1972.
[37] A. Bhattacharya, WO/1992/04965.
[38] R.D. Shannon, Acta Crystallogr. A 32 (1976) 751.
[39] R.D. Shannon, C.T. Prewitt, Acta Crystallogr. B 25 (1969) 925.
[40] B. Visnawathan, Catal. Rev. Sci. Eng. 34 (1992) 337–354.
[41] F. Dong, A. Suda, T. Tanabe, Y. Nagai, H. Sobukawa, H. Shinjoh, M. Sugiura, C. Descorme, D. Duprez, Catal. Today 93–95 (2004) 827–832.
[42] S. Royer, D. Duprez, S. Kaliaguine, J. Catal. 234 (2005) 364–375.
[43] I.L. Zhogin, A.P. Nemudry, P.V. Glyanenko, Y.M. Kamenetsky, H.J.M. Bouwmeester, Z.R. Ismagilov, Catal. Today 118 (2006) 151–157.
[44] T.X.T. Sayle, S.C. Parker, D.C. Sayle, Faraday Discuss. 134 (2007) 377–397.
[45] Z. Song, H. Nishiguchi, W. Liu, Appl. Catal. A 306 (2006) 175–183.